the plant journal

SEB Society for Experimental Biology

The Plant Journal (2014) **77,** 806–814 doi: 10.1111/tpj.12429

TECHNICAL ADVANCE

The iRoCS Toolbox – 3D analysis of the plant root apical meristem at cellular resolution

Thorsten Schmidt[1,*], Taras Pasternak[2], Kun Liu[1], Thomas Blein[2,†], Dorothée Aubry-Hivet[2], Alexander Dovzhenko[2,3], Jasmin Duerr[2], William Teale[2], Franck A. Ditengou[2], Hans Burkhardt[1,4], Olaf Ronneberger[1,4] and Klaus Palme[2,4,5,6]

[1]*Institute for Computer Science, Albert Ludwigs University Freiburg, Georges Köhler Allee, Gebäude 52, D–79110 Freiburg, Germany,*

[2]*Institute for Biology II, Albert Ludwigs University Freiburg, Schänzlestraße 1, D–79104 Freiburg, Germany,*

[3]*Center for Applied Biosciences (Zentrum für angewandte Biowissenschaften), Albert Ludwigs University Freiburg, Sonnenstraße 5, D–79104 Freiburg, Germany,*

[4]*Centre for Biological Signalling Studies, Albert Ludwigs University Freiburg, Signalhaus, Schänzlestraße 18, D–79104 Freiburg, Germany,*

[5]*Freiburg Centre for Advanced Studies, Albert Ludwigs University Freiburg, Albertstraße 19, D–79104 Freiburg, Germany, and*

[6]*Freiburg Initiative for Systems Biology, Faculty for Biology, Albert Ludwigs University Freiburg, Albertstraße 19, D–79104 Freiburg, Germany*

Received 20 July 2012; revised 16 December 2013; accepted 23 December 2013; published online 13 January 2014.

*For correspondence (e-mail tschmidt@cs.uni-freiburg.de).

†Present address: Institut National de la Recherche Agronomique, UMR1318, Institut Jean-Pierre Bourgin, RD10, F–78000 Versailles, France and AgroParisTech, Institut Jean-Pierre Bourgin, RD10, F–78000 Versailles, France.

SUMMARY

To achieve a detailed understanding of processes in biological systems, cellular features must be quantified in the three-dimensional (3D) context of cells and organs. We described use of the intrinsic root coordinate system (iRoCS) as a reference model for the root apical meristem of plants. iRoCS enables direct and quantitative comparison between the root tips of plant populations at single-cell resolution. The iRoCS Toolbox automatically fits standardized coordinates to raw 3D image data. It detects nuclei or segments cells, automatically fits the coordinate system, and groups the nuclei/cells into the root's tissue layers. The division status of each nucleus may also be determined. The only manual step required is to mark the quiescent centre. All intermediate outputs may be refined if necessary. The ability to learn the visual appearance of nuclei by example allows the iRoCS Toolbox to be easily adapted to various phenotypes. The iRoCS Toolbox is provided as an open-source software package, licensed under the GNU General Public License, to make it accessible to a broad community. To demonstrate the power of the technique, we measured subtle changes in cell division patterns caused by modified auxin flux within the *Arabidopsis thaliana* root apical meristem.

Keywords: *Arabidopsis thaliana*, root modelling, automated image analysis, confocal microscopy, population studies, pin mutants, technical advance.

INTRODUCTION

Due to recent advances in non-invasive optical sectioning, three-dimensional (3D) imaging of plant roots at cellular resolution is now routine (Shaw and Ehrhardt, 2013). However, image analysis has not undergone similar development, with cellular annotation of images remaining laborious, time-intensive work that is by no means routine. Accordingly, a wealth of detailed phenotypic information is typically passed over in favour of analysing relatively strong phenotypes. A platform that is able to dramatically cut the time it takes to robustly annotate roots would allow routine analysis of relatively mild phenotypes, and clear the way for the robust

© 2014 The Authors
The Plant Journal © 2014 John Wiley & Sons Ltd

association of signalling pathways with mild developmental effects.

In zoology, descriptive atlases are well established, and have been applied to a wide range of model organisms, including the mouse (Mus) (Lein *et al.,* 2007; Dorr *et al.*, 2008), zebrafish (*Danio Rerio*) (Ronneberger *et al.*, 2012), fruit fly (*Drosophila*) (Luengo Hendriks *et al.*, 2006; Fowlkes *et al.* 2008) and nematodes (*Caenorhabditis elegans*) (Long *et al.*, 2009). However, such inflexible models are not suitable for description of plant anatomy, which has evolved extreme plasticity in response to the evolutionary pressure of a sessile lifestyle. Even for single organs, such as the root tip, a one-to-one mapping to a reference atlas is precluded by high heterogeneity between individuals.

Previous attempts to exploit the rotational symmetry of root tips to obviate these difficulties and streamline the annotation process have invariably made compromises, either with respect to the total amount of data analysed, by restricting the analysis to selected 2D sections (Santuari *et al.*, 2011; Federici *et al.*, 2012), or with respect to the resolution of the annotation, by projection of the 3D data onto a 2D plane (Ubeda-Tomás *et al.*, 2009). Projections allow integrative analyses without data loss. However, information from different tissues and cell files are combined, which precludes cell fate-specific differential analyses.

Here we introduce a method that enables direct annotation and analysis of reconstructed 3D images of Arabidopsis roots without artificial reduction to 2D. We extend existing descriptions of root geometry by introduction of biologically meaningful discrete quantities: cell layers and cell files (Sena *et al.*, 2011). This additional distinction, coupled with automation of the pipeline, allows detailed differential analyses of the root apical meristem (RAM). We call the resulting model the intrinsic root coordinate system (iRoCS).

The regulation of auxin transport is an ideal framework by which to test the accuracy of root analysis systems. The Arabidopsis genome encodes eight PIN proteins, most of which have been shown to influence root development (Friml *et al.*, 2002; Paponov *et al.*, 2005; Petrášek *et al.*, 2006). Of these, PINs 1, 3, 4 and 7 are located in the stele and act redundantly (Blilou *et al.*, 2005) to influence the activity of PLETHORA (PLT): an auxin-responsive transcription factor that controls root growth (Aida *et al.*, 2004). Another PIN protein, PIN2, mediates the epidermal flow of auxin away from the root tip to influence the root's gravitropic response (Müller *et al.*, 1998) (Figure S1). As single knockout mutants of the corresponding *PIN* genes cause relatively subtle root phenotypes, they were used to test the power of iRoCS.

iRoCS enables researchers to rapidly standardize their data within a single framework, and quantitatively compare cohorts of roots. Its associated algorithmic pipelines automatically recognize cell boundaries and nuclei, drastically reducing the time required to fully annotate a single root. This time saving enables large cohorts of roots to be annotated, making statistical analyses possible and enabling unbiased evaluation of previously hidden, mild developmental phenotypes.

RESULTS AND DISCUSSION

The intrinsic root coordinate system

Analysis of developmental events in the context of a whole organ requires transformation of their recorded positions from the Euclidean recording coordinate system into root-intrinsic coordinates (Figure 1a). A natural choice is use of cylinder coordinates originating in the quiescent centre (QC), with three dimensions: for points apical to QC z is (chosen to be) negative, the orthogonal distance to the axis (r) and the angle around the axis (ϕ). Any Euclidean position may be uniquely transformed into this coordinate system, allowing comparison of root populations. The locations and appearances of the cells are used to determine their fate and provide each cell with two additional discrete coordinates, namely the cell's tissue layer and file. These discrete coordinates are the basis for root atlases for various plant species, which distinguish the various tissues and sub-divide them into cell lineages. An immediate application of iRoCS, which exploits this combination of discrete and continuous coordinates, is a virtually 'unrolled' root visualization revealing the root's internal structure (Figure 1b).

Applications

iRoCS is a general tool that has a wide spectrum of possible applications at various detail levels, ranging from whole-organ descriptions to detection of subtle changes in cellular architecture. Independent of the marked anatomical structures (nuclei/cell boundaries), all roots share the same coordinate system, which, for the first time, allows direct comparison of individual plants and population studies in 3D at cellular resolution. This requires recording of high-resolution 3D image stacks and processing them first automatically and then manually until the annotation quality required by the experiment is reached. iRoCS analyzes phenotypic differences that are commonly hidden by natural variation among individual plants.

The iRoCS pipeline

The coordinate system may be manually fitted to each individual root, but the iRoCS Toolbox provides a way of largely automating this process, providing different views of the cellular architecture of the roots based on 3D microscopic recordings (Documentation D1). It comprises two pipelines to process data based on nuclear or cell-boundary (membrane/cell wall) markers. Both pipelines comprise detection of the basic structures (nuclei/cell boundaries),

© 2014 The Authors

1365313x, 2014, 5, Downloaded from https://onlinelibrary.wiley.com/doi/10.1111/tpj.12429 by Cochrane France, Wiley Online Library on [21/10/2026]. See the Terms and Conditions (https://onlinelibrary.wiley.com/terms-and-conditions) on Wiley Online Library for rules of use; OA articles are governed by the applicable Creative Commons License

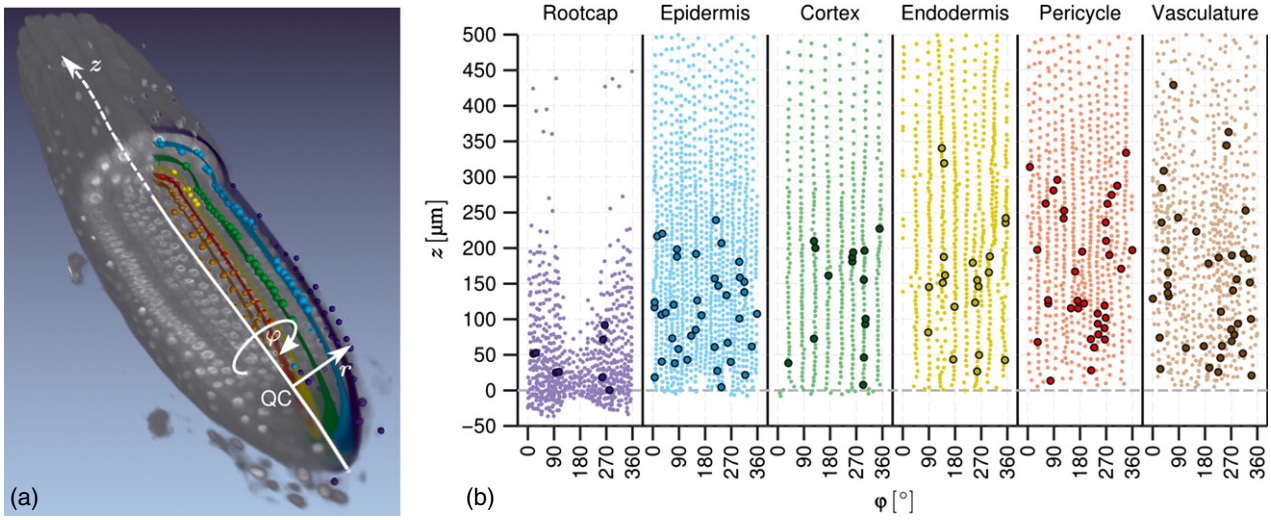

Figure 1. Root description using iRoCS.
(a) Volume rendering of a DAPI-stained Arabidopsis root tip virtually cut along the root axis. White annotations indicate the attached cylinder coordinate system; coloured spheres indicate nuclei of different tissue layers.
(b) Nucleus map of a virtually unrolled wild-type root sample with accumulated mitoses after 60 min colchicine treatment. Each sub-graph corresponds to the indicated tissue layer. Dots, cell nuclei; circles, mitoses.

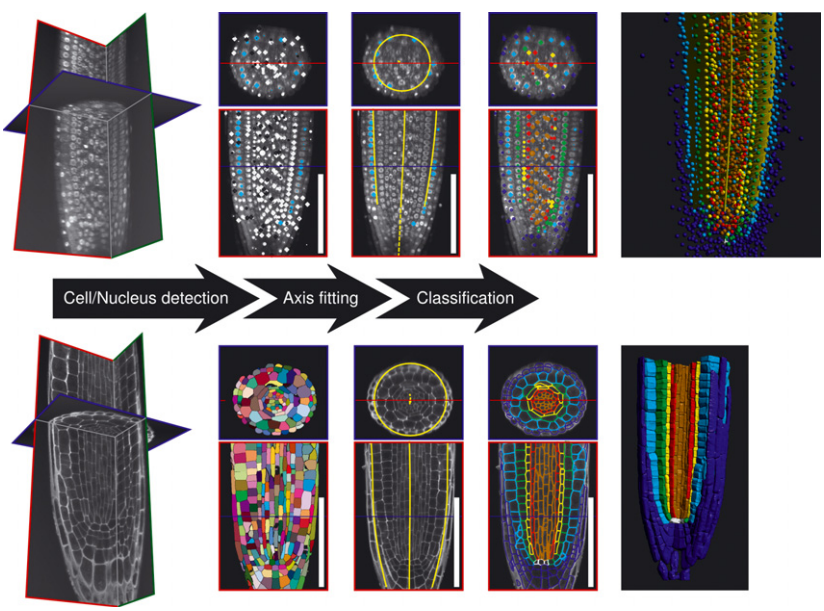

Figure 2. iRoCS pipelines.
Top: nucleus-based pipeline; bottom: cell boundary-based pipeline. From left to right: orthographic view of the microscopic recording; feature detection result in *xy* and *zy* sample slices (top: nucleus locations; bottom: cell segmentation); axis fitting result (yellow lines indicate the centre line and mean root thickness); classification of the cells by tissue layer (dark blue, root cap; cyan, epidermis; green, cortex; yellow, endodermis; red, pericycle; brown, vasculature; white, QC); 3D rendering of the resulting model. Scale bars = 100 µm.

definition of the coordinate system, and assignment of a layer label to each cell. This process is shown in Figure 2.

To fit the coordinate system, the coordinate origin (QC) must be manually annotated for each root, which requires minimal user interaction. The output tables of both pipelines contain different properties for each cell, which depend on the type of input data provided. Independent of the marker, the positions of all cells as Euclidean coordinates and bent-cylinder coordinates are extracted. The whole pipeline is described in Experimental procedures, and in more detail in the Methods S1–S3. The accuracy of the automatic analysis depends on the quality of the input data. For good data quality, detection of the basic structures is usually more than 90% accurate (Figure S2), but errors in this step affect the accuracy of all further steps. Detailed detection, segmentation and classification accuracy analyses are described in Methods S1 and S3.

Nucleus detection and classification (semi-automatic). Staining of nuclei using 4,6–diamidino-2–phenylindole (DAPI) resulted in a variety of appearances. Therefore, simultaneous detection of nuclei at various developmental

© 2014 The Authors

1365313x, 2014, 5, Downloaded from https://onlinelibrary.wiley.com/doi/10.1111/tpj.12429 by Cochrane France, Wiley Online Library on [21/10/2026]. See the Terms and Conditions (https://onlinelibrary.wiley.com/terms-and-conditions) on Wiley Online Library for rules of use; OA articles are governed by the applicable Creative Commons License

stages is hard to perform automatically (Figure 3). Simple hand-crafted detection filters such as the well-known Laplacian of Gaussian (LoG) filter used in the scale invariant feature transform (SIFT) described by Lowe (2004) cannot cope with this variety. Instead, we provide a trainable detector that learns any nuclear appearance of the analysed species from annotated training roots. To detect nuclei in all possible orientations, we extract rotation-invariant numerical descriptions (referred to below as 'features') of their local appearance (Methods S1.1). The individual features are combined into feature vectors. We use Laguerre/Gaussian-type basis functions as described by Skibbe *et al.* (2012), and transform the intensities around each nucleus centre. The magnitudes of the tensorial coefficients corresponding to low angular frequencies are computed and assembled to an initial feature vector. This is repeated on eight scales with exponentially increasing radial range. Then, we extend the feature vector using the vectorial invariants described by Schulz *et al.* (2006). To obtain nucleus location hypotheses, we extract the local maxima of the decision values of a voxel-wise classification using a two-class support vector machine (Vapnik, 1998). More details on the detection process are given in Methods S1.2.

In the later pipeline steps, the extracted features are re-used to classify the detected nucleus candidates into the classes 'epidermis', 'other nucleus' and 'background' using a multi-class support vector machine (Methods S1.4 and Table S1). A bent-cylinder coordinate system is fitted to the epidermis using the coupled curves model described by Schmidt *et al.* (2012) (Methods S2). A final classification assigns a layer label and a mitotic state to each cell. This classification uses the continuous bent cylinder coordinates as additional features (Methods S3 and Table S2).

Due to direct use of the coordinates, this step only works accurately for mild phenotypes. For more severe phenotypes the SVM model for layer assignment needs to be retrained. However, it is possible to use the initial output as a starting point to manually correct erroneous layer assignments rather than performing a full annotation. The corrected samples may then be used directly for re-training if more roots of the phenotype need to be analysed, which is very likely in the case of population studies. All roots used for the statistical evaluations presented were classified using only a single model trained on the wild-type.

Figure 1(b) shows the nucleus positions for a virtually unrolled root for each layer. In the outer cell layers (epidermis to pericycle), the single cell files may be clearly distinguished as axially oriented chains of nuclei.

Cellular root segmentation (automatic). The cell boundary pipeline decomposes the image volume into (a set of) non-overlapping segments (ideally one segment per cell). For each segment, the position of its centre of mass in Euclidean and cylinder coordinates, its volume and its tissue layer are determined. The iRoCS Toolbox allows editing of the cell layer and file assignment. Over-segmentations (when cells are split into multiple parts) may be corrected by simply indicating the segments to be merged. Correction of under-segmentations would require full manual annotation of missing cell boundaries in 3D, which is very time-consuming and error prone. Such functionality is not part of the iRoCS Toolbox. If a segment contains more than one cell, the iRoCS Toolbox allows removal of the segment so as not to harm the later analysis. Therefore, the segmentation parameters should be adjusted to obtain slight over-segmentation if perfect segmentation is not achieved by any parameter set-up.

Figure 4 shows a surface rendering of a sample segmentation result on a wild-type root after applying the pseudo-Schiff propidium iodide staining technique described by Truernit *et al.* (2008). The proposed segmentation approach also robustly delineates cells using cell membrane markers (Methods S1.3 and Figure S3). Note that no additional root clearing was applied for the membrane-based segmentation.

Root registration (automatic). Independent of the pipeline used, the extracted coordinates (z, r and ϕ) allow

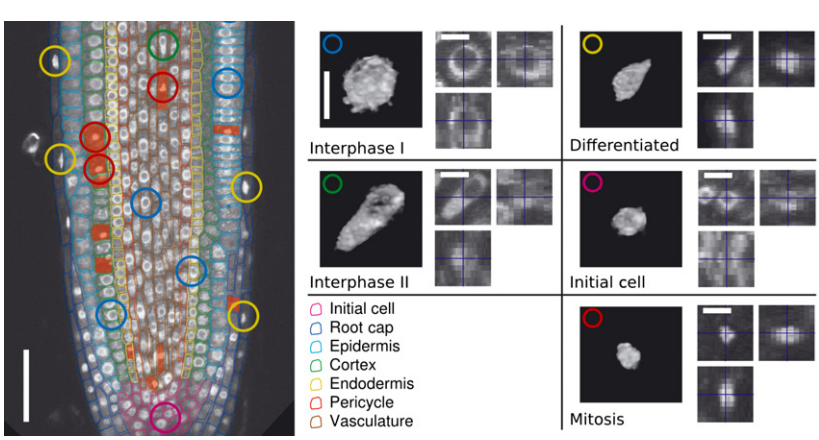

Figure 3. Nuclear appearances for various developmental stages.
Left: *xy* cut through a DAPI-stained Arabidopsis root tip. Coloured lines: manually added cell outlines; circles: sample nuclei of the various morphological classes. Red shading indicates mitoses. Scale bar = 50 μm.
Right: each box shows a volume rendering of a single cell of the indicated type on the left, and orthographic (*xy*, *xz* and *zy*) cuts through that nucleus on the right. Scale bars = 10 μm.

© 2014 The Authors

1365313x, 2014, 5, Downloaded from https://onlinelibrary.wiley.com/doi/10.1111/tpj.12429 by Cochrane France, Wiley Online Library on [21/10/2026]. See the Terms and Conditions (https://onlinelibrary.wiley.com/terms-and-conditions) on Wiley Online Library for rules of use; OA articles are governed by the applicable Creative Commons License

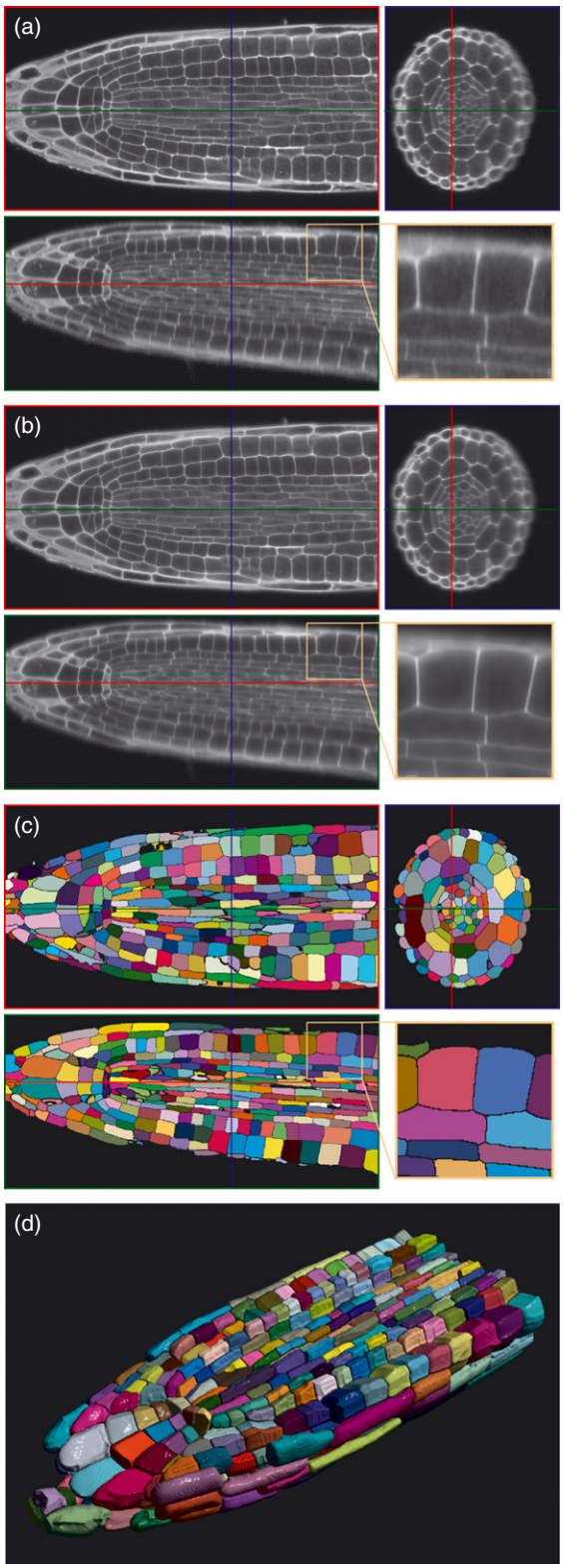

Figure 4. Automatic cell wall-based segmentation.
(a) Raw data; (b) enhanced image after anisotropic diffusion; (c) segmented cells with random colour coding; (d) surface rendering of cells of half of the root virtually cut along an axial plane. Coloured lines indicate virtual sections. Scale bars = 100 μm.

comparison of the locations of events in various plants or plant populations with respect to the distance to the QC and the lateral distance from the root axis. Typical iRoCS registration results are shown in Figure S4, and more details on the iRoCS fitting process are given in Methods S2. The pipeline initially places the zero angle of the ϕ dimension arbitrarily, and all angles are given relative to this zero angle. If registration along the ϕ dimension is required, the user must define a reference angle, which may either depend on anatomical cues or the higher-level root geometry.

Mitosis distribution analysis (semi-automatic). Cell divisions are rare events in the Arabidopsis root (only 1–3% of root tip cells are in the M phase of the cell cycle at any time point), and are restricted to the RAM with the exception of lateral root initiation (Malamy and Benfey, 1997). In order to draw statistically significant conclusions on differences in the mitosis distributions among different populations, large sample sizes must be fully recorded and analysed in 3D. We used DAPI to visualize the DNA within the samples. To additionally increase the number of observable mitotic events, we hampered the transition to anaphase by incubation with colchicine, which was applied for 30, 60 or 90 min prior to fixation. This treatment has two effects: first, cells entering metaphase during the incubation period accumulate, and second, the visual appearance of mitoses becomes more coherent, i.e. the chromosomes form unstructured but very dense agglomerates, replacing the normally visible mitotic plates or spindles. The incubation period chosen was very short compared to the entire duration of the cell cycle [between 19 h (Beemster and Baskin, 1998) and 48 h (Fujie *et al.*, 1993)] in order to avoid side-effects.

We applied the iRoCS pipeline to samples from three populations: wild-type, *pin2* and *pin4*. For each group, we recorded at least ten samples, marked their QC positions and manually corrected classification errors of a random subset of 10 samples from each population with respect to the tissue layer and mitotic state. Sample nucleus maps for individual sample roots and mitosis distribution histograms for the populations are shown in Figure 5(a–c). As the auxin flux controlled by the PINs affects the various layers differently, we estimated the mitosis distributions along the root axis for each layer independently (Figure 5d).

As expected, *pin4* shows no significant differences in the distribution of mitoses compared to the wild-type. This is attributed to the high redundancy of the PIN network in the stele. However, the detailed analysis reveals significant differences in the mitosis distribution in the vasculature for *pin2*. The mitosis distributions in the stele are shifted towards the root tip, whereas the outer layers show no significant changes. However, a slight distribution shift is observed in the cortex layer towards the shoot. The

© 2014 The Authors

1365313x, 2014, 5, Downloaded from https://onlinelibrary.wiley.com/doi/10.1111/tpj.12429 by Cochrane France, Wiley Online Library on [21/10/2026]. See the Terms and Conditions (https://onlinelibrary.wiley.com/terms-and-conditions) on Wiley Online Library for rules of use; OA articles are governed by the applicable Creative Commons License

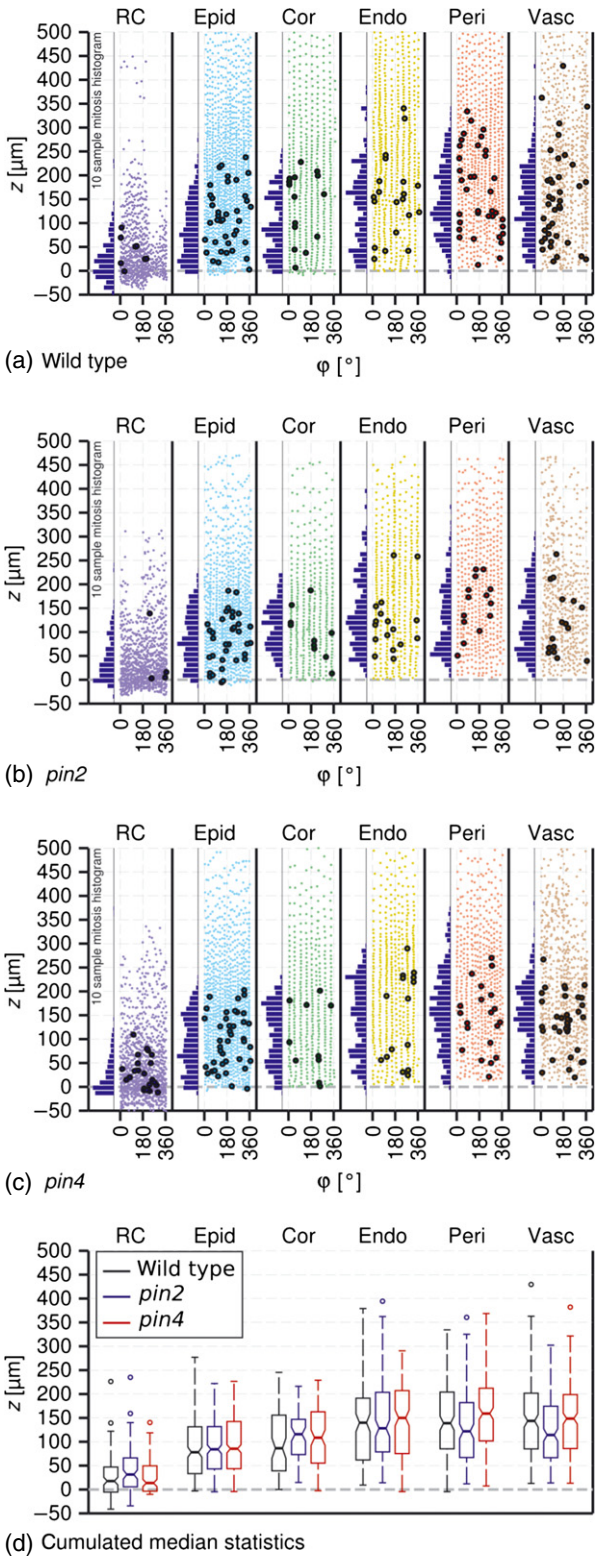

Figure 5. Comparison of per layer mitosis distributions for three populations (n = 10 for each population). RC, root cap; Epid, epidermis; Cor, cortex; Endo, endodermis; Peri, pericycle; Vasc, vasculature.
(a–c) Representative nucleus maps of virtually unrolled root tips. Dots, nuclei; circles, mitoses. The histogram to the left of each layer panel indicates the mitosis distribution of that layer for the plant population: (a) wild-type; (b) *pin2*; (c) *pin4*. (d) Summary of the mitosis distributions of the three populations. Bars: median values; boxes: interquartile ranges (IQR); whiskers: lowest and highest data within 1.5 IQR; open circles: outliers. Notches at either side of the boxes around the median bar indicate significance of differences of the distribution medians using the non-parametric Kruskal–Wallis test. Non-overlapping notch intervals indicate significantly different medians (P = 0.05).

reasons for these differences require further analysis, but the reduced auxin efflux in the epidermis of *pin2* appears to significantly alter the auxin gradient in the stele. Ottenschläger *et al.* (2003) have demonstrated auxin accumulation in root tips of *pin2* plants. However, the increase is most prominent in columella. To our knowledge, a significant effect on the stele has not yet been observed.

For comparison, the nucleus maps and corresponding box plots for a fully automatic analysis are given in Figure S5. The observed differences are discussed in Methods S4.

Adaptation to strong phenotypes (semi-automatic). iRoCS may be easily adapted to strong phenotypes. To show this, we analysed the distribution of nuclei in the *shortroot* (*shr*) mutant. The *SHORTROOT* (*SHR*) gene plays a central role in controlling the asymmetric cell divisions of the cortex/endodermis initials. The endodermis is not developed and therefore absent in *shr* plants (Cui *et al.*, 2007). The *shr* phenotype is characterized by very short roots and darker cotyledons compared to the wild-type (Helariutta *et al.*, 2000).

Preparation and recording were performed as described in Experimental procedures without application of colchicine. We applied the iRoCS pipeline using models for nucleus detection and epidermis labelling trained on the wild-type. These models are not affected by the *shr* phenotype because the nuclear appearance remains the same and the epidermis is still the outer root layer.

Only the layer assignment model (which relies on the root geometry) was re-trained. This was necessary because *shr* has a shorter and thinner RAM, and the endodermal layer is absent. To do this, the layers were first classified using the layer assignment model trained on the wild-type. Stele had already been accurately assigned using this model. Erroneous labels in the outer tissues were manually corrected, and the new model was trained using correctly assigned layer labels (Methods S5 and Table S3).

Figure 6(a) shows the resulting nucleus map and corresponding mitosis distribution for a *shr* population comprising four roots. When comparing the nuclear density and mitosis distributions of *shr* mutants with other genotypes in the z direction, the RAM shortening is clearly visible. The mean RAM lengths of the various populations were compared after fitting a bi-sigmoidal model to the measured cellular positions (Methods S6 and Figures S6–S8). The comparison is shown in Figure 6(b).

© 2014 The Authors

1365313x, 2014, 5, Downloaded from https://onlinelibrary.wiley.com/doi/10.1111/tpj.12429 by Cochrane France, Wiley Online Library on [21/10/2026]. See the Terms and Conditions (https://onlinelibrary.wiley.com/terms-and-conditions) on Wiley Online Library for rules of use; OA articles are governed by the applicable Creative Commons License

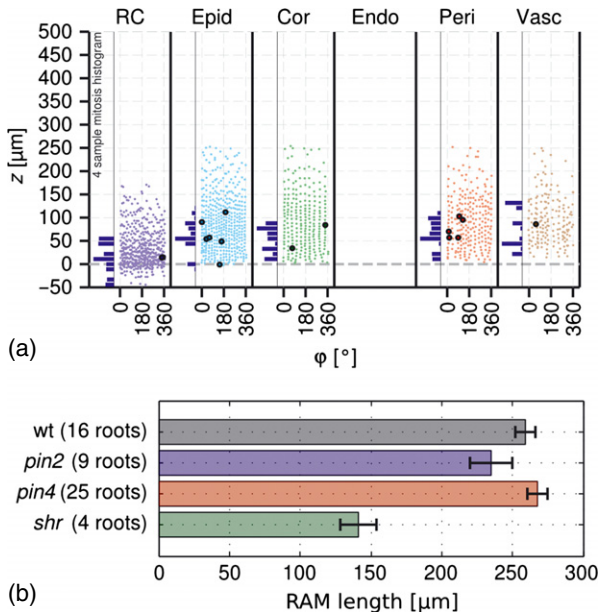

Figure 6. Application of iRoCS to samples of the *shortroot* (*shr*) mutant.
(a) Sample nucleus locations of one *shr* root tip. Dots, nuclei; circles, mitoses. The histogram to the left of each layer panel indicates the mitosis distribution of that layer for the plant population. RC, root cap; Epid, epidermis; Cor, cortex; Endo, endodermis; Peri, pericycle; Vasc, vasculature.
(b) Comparison of the mean RAM lengths of wild-type, *pin2*, *pin4* and *shr*. Error bars indicate SE.

The wild-type and *pin4* RAMs were not significantly different in length [259.1 ± 7.2 µm (n = 16) and 267.5 ± 7.1 µm (n = 25), respectively; $P_{wt/pin4}$ = 0.43). The *pin2* RAM is slightly shorter [235.1 ± 14.7 µm (n = 9); $P_{wt/pin2}$ = 0.11, $P_{pin2/pin4}$ = 0.04). In accordance with its known phenotype, *shr* has a significantly shorter RAM [141.1 ± 13.1 µm (n = 4); $P_{wt/shr} = 6 \times 10^{-7}$, $P_{pin2/shr}$ = 0.002, $P_{pin4/shr} = 3 \times 10^{-7}$). As a statistical test, we used pairwise ANOVA (one-way analysis of variance). All length measurements are means ± standard error (SE) with indicated population sizes.

CONCLUSION

iRoCS may be applied in a wide spectrum of studies, ranging in scale from whole organs to subcellular analyses. The description of events within the framework of a root intrinsic coordinate system enables analyses not only on individual plants, but on plant populations, making use of the 3D information contained in the samples. This reduces plant preparation time and facilitates in-depth plant analysis.

In principle, the design of the iRoCS Toolbox allows application to root meristems of other species. When using a nuclear marker, the detector needs to be trained. The training involves annotation of nuclei for a small sample of root tips to teach the software the morphological appearance of the nuclei of that species. We used two Arabidopsis root tips for our findings; the corresponding detector model may be downloaded from the project website http://lmb.informatik.uni-freiburg.de/lmbsoft/iRoCS. When using a cell boundary marker, delineation of the cells does not require an additional training step, and the system segments the root automatically into its individual cells. As the layered architecture differs between different species or even within a species for specific mutants (e.g. *shr* lacks the endodermis in Arabidopsis), manual annotation of the layers is required for a few samples to teach the system the specific root architecture of that species/mutant. However, this annotation may be initialized by the pipeline result using a sub-optimal model, so that only local corrections are required instead of a full annotation. Once a few root samples have been annotated, the specific models may be trained and arbitrarily applied to many additional roots of similar phenotype. To define the coordinate origin of iRoCS, the quiescent centre must be marked for all samples, which is the only required manual step for the analysis. All further automatic steps may be reviewed and revised if necessary. This gives full control to the user, ensuring expert-level data quality.

EXPERIMENTAL PROCEDURES

Sample preparation and recording

Seeds were surface-sterilized and sown on square Petri dishes containing half-strength Murashige and Skoog medium containing vitamins, 0.5% sucrose and 1% w/v agar (Roth, http://www.carlroth.com). The dishes were kept at room temperature for 4 h before transfer to 4°C for 12 h. Dishes were then transferred to 22°C under long-day conditions for the next 60 h (13 light, 8 dark, 16 light, 8 dark, 15 light). After scanning the dishes using a Canon F950 scanner (http://www.canon.com), the primary root length was measured using Scion Image (Scion Corporation, http://scion-image.software.informer.com). To ensure a comparable developmental age, only seedlings with root lengths of 8mm (p/m 10%) were further processes. They were transferred to a 24-well plate containing liquid half-strength Murashige and Skoog medium with vitamins and 0.5% sucrose) for 12 h. Colchicine was then added (final concentration 0.1% w/v), and plants were incubated for either 30, 60 or 90 min. After incubation, the plants were fixed in 2% w/v formaldehyde in microtubule stabilization buffer for 30 min. Then the plants were washed twice with distilled water for 10 min, incubated in DAPI (200 µg L^{-1}) for 20 min, washed again with distilled water, and mounted on slides using a 120 µm spacer and Fluoromount G (Southern Biotechnology Inc., http://www.southernbiotech.com) as the embedding medium.

The DAPI-stained root tips were imaged using a confocal laser scanning microscope (LSM 510 Duo Live; Zeiss, http://www.zeiss.com) at an excitation wavelength of 405 nm with a C–Apochromat 40 x/1.2 W corrected UV-VIS-IR objective (Art.-No. 441757-9970-000). Serial optical sections were reconstituted into 3D image stacks to a depth of 100 µm, with an in-plane sampling of 0.15 µm and a section spacing of 1 µm. Two or three partially overlapping image stacks were recorded for each root.

Consecutive image stacks were stitched to a total length of 500 µm from the QC using XuvTools (Emmenlauer *et al.*, 2009). Liquid embedding may induce small root rotations that cannot be

© 2014 The Authors

1365313x, 2014, 5, Downloaded from https://onlinelibrary.wiley.com/doi/10.1111/tpj.12429 by Cochrane France, Wiley Online Library on [21/10/2026]. See the Terms and Conditions (https://onlinelibrary.wiley.com/terms-and-conditions) on Wiley Online Library for rules of use; OA articles are governed by the applicable Creative Commons License

resolved using the strict translational model of XuvTools; therefore datasets with errors exceeding 10 μm at the stitching boundary were discarded. The stitching error does not influence the mitosis distributions, because the proliferation zone was fully included in the first tile. The goal of the stitching was to ensure that no mitoses in the region distal from the QC were missed. For description of more distal events, the root must be mechanically fixed to the cover slip.

The method used for cell-wall propidium iodide staining was adapted from that described by Truernit *et al.* (2008). Plants were fixed in 50% methanol and 10% acetic acid and stored at 4°C until use. After progressive rehydration, an overnight amylase treatment at 37°C (20 mM Na-phosphate buffer, pH 7, supplemented with 2 mM NaCl, 0.25 mM $CaCl_2$ and 0.01% amylase) was performed as described previously (Wuyts *et al.*, 2010). After rinsing in water, the roots were incubated for 40 min in 1% periodic acid at room temperature. After a further rinse in water, the seedlings were incubated in pseudo-Schiff reagent with propidium iodide (100 mM sodium metabisulphite and 0.15 N HCl; propidium iodide was freshly added to a final concentration of 0.1 mM) for 15 min. The samples were then rinsed in water before incubation for 1 h in 10% glycerol and then for 1 h in mounting solution (80 g chloral hydrate in 27 ml H_2O, 3 ml glycerol). After an overnight incubation in new mounting solution, the samples were mounted on slides surrounded by a 120 μm thick frame to avoid root squeezing.

The propidium iodide-stained roots were imaged using a confocal laser scanning microscope (LSM 510; Zeiss) at an excitation wavelength of 488 nm with a Plan-Neofluar 40 x/1.3 Oil objective. Serial optical sections were reconstituted into 3D image stacks to a depth of 100 μm, with in-plane sampling of 0.4 μm and section spacing of 0.4 μm.

For all recordings, the microscope was set-up for optimal use of the available 12 bit intensity range (grey values: [0, 4096]).

Nucleus detection/classification training

For detector training, the nucleolus radius, cell layer, cell file and division status of nuclei in the cells of two root tips were manually annotated. If multiple nucleoli were visible, the most prominent was chosen. For performance evaluation of the trained detector, detections within a 3 μm radius around a nucleus centre were regarded as true positive detections. In the case of multiple detections of the same nucleus, only the detection with highest probability score was retained, and the remainder were regarded as false positives. The classifier used was a soft margin support vector machine with a radial basis function kernel (Vapnik, 1998). To estimate the outlier penalty cost C and kernel width γ, we performed a twofold cross-validation. We then trained the nucleus detector model on both datasets and applied the nucleus detection to six additional wild-type roots. The resulting nucleus candidates were manually validated, and, where necessary, re-labelled according to tissue layer and mitotic state. The epidermis labelling and layer assignment models were trained on this extended set of eight roots. The support vector machine parameters were determined using a 'leave one out' cross-validation beforehand. The training set was strictly separate from the analysed root database to avoid experimental bias in the statistical results.

The cellular segmentation of samples with marked cell boundaries was performed fully automatically without training for a specific species. Assuming thin cell walls, it is even independent of the choice of the boundary structure labelled, i.e. either cell walls or membranes may be used for the segmentation task (Figure 4 and Figure S3). The segmentation consists of an edge-enhancing pre-processing step (anisotropic diffusion filtering), then edge detection, and finally watershed segmentation. More details and a detailed evaluation of the various steps are given in Methods S2.3.

Definition of the coordinate system

For definition of the bent-cylinder coordinate system, we used the coupled curves model described by Schmidt *et al.* (2012). The model was initialized using a seed cylinder. The orientation and diameter of this cylinder were automatically determined from an ellipsoid fit to the epidermis nucleus positions. The initial length of the seed cylinder was set to 20% of the length of the main axis of the ellipsoid. For cell boundary markers, the first classification is omitted and the fit is directly performed on the perimeter pixels of the root (the union of the detected cells).

The distance z of a point from the QC is given by the curve length between the manually annotated QC and the point's projection onto the axis. The lateral distance r is the length of this projection vector. The angle ϕ is determined relative to the recording direction (Methods S2.4).

Cell layer assignment

For nuclear markers, the features used for detection and epidermis labelling were re-used. For cell boundary markers, shape features for each cell were extracted. As features, we used the distances of the segment boundary points to the segment centre in 32 directions relative to the iRoCS orientation. This classification uses the continuous bent-cylinder coordinates as additional features.

ACKNOWLEDGEMENTS

We thank the members of our teams for helpful comments on the manuscript. We also gratefully acknowledge excellent technical support from Roland Nitschke (Life Imaging Centre, Zentrum für Biosystemanalyse, Freiburg, Germany). This work was supported by Collaborative Research Center 746, the Excellence Initiative of the German Federal and State governments (EXC 294), the European Space Agency, the Bundesministerium für Bildung und Forschung (0315329 and 0315690), and the Deutsches Zentrum für Luft- und Raumfahrt. We finally wish to gratefully acknowledge EMBO for the long-term postdoctoral fellowship awarded to T.B.

SUPPORTING INFORMATION

Additional Supporting Information may be found in the online version of this article.

Figure S1. PIN protein localization within the Arabidopsis RAM.
Figure S2. Nucleus detection evaluation.
Figure S3. Automatic cell membrane-based segmentation.
Figure S4. Qualitative evaluation of root axis fitting.
Figure S5. Fully automatic mitosis distribution analysis.
Figure S6. The bi-sigmoid axial cell density model.
Figure S7. Cumulative cell counts for the individual roots of the four analysed populations.
Figure S8. Summary of the cell densities and the cumulative cell count for the four analysed populations.

Table S1. Classification accuracy of the epidermis labelling.
Table S2. Classification accuracy of the layer assignment.
Table S3. Classification accuracy of the *shr* layer assignment after re-training.

Methods S1. Cell/nucleus detection.
Methods S2. iRoCS fitting.
Methods S3. Evaluation of the cell layer assignment.
Methods S4. Mitosis distribution analysis (automatic).
Methods S5. Evaluation of the layer assignment for *shr*.

© 2014 The Authors

1365313x, 2014, 5, Downloaded from https://onlinelibrary.wiley.com/doi/10.1111/tpj.12429 by Cochrane France, Wiley Online Library on [21/10/2026]. See the Terms and Conditions (https://onlinelibrary.wiley.com/terms-and-conditions) on Wiley Online Library for rules of use; OA articles are governed by the applicable Creative Commons License

Methods S6. RAM length estimation.
Documentation D1. The iRoCS Toolbox: short user's guide.

REFERENCES

Aida, M., Beis, D., Heidstra, R., Willemsen, V., Blilou, I., Galinha, C., Nussaume, L., Noh, Y. S., Amasino, R. and Scheres, B. (2004) The PLETHORA genes mediate patterning of the Arabidopsis root stem cell niche. *Cell*, **119**, 109–120.

Beemster, G.T.S. and Baskin, T.I. (1998) Analysis of cell division and elongation underlying the developmental acceleration of root growth in *Arabidopsis thaliana*. *Plant Physiol.* **116**, 1515–1526.

Blilou, I., Xu, J., Wildwater, M., Willemsen, V., Paponov, I., Friml, J., Heidstra, R., Aida, M., Palme, K. and Scheres, B. (2005) The PIN auxin efflux facilitator network controls growth and patterning in Arabidopsis roots. *Nature*, **433**, 39–44.

Cui, H., Levesque, M.P., Vernoux, T., Jung, J.W., Paquette, A.J., Gallagher, K.L., Wang, J.Y., Blilou, I., Scheres, B. and Benfey, P.N. (2007) An evolutionarily conserved mechanism delimiting SHR movement defines a single layer of endodermis in plants. *Science*, **316**, 421–425.

Dorr, A.E., Lerch, J., Spring, S., Kabania, N. and Henkelman, R.M. (2008) High resolution three-dimensional brain atlas using an average magnetic resonance image of 40 adult C57BL/6J mice. *Neuroimage*, **42**, 60–69.

Emmenlauer, M., Ronneberger, O., Ponti, A., Schwarb, P., Griffa, A., Filippi, A., Nitschke, R., Driever, W. and Burkhardt, H. (2009) XuvTools: free, fast and reliable stitching of large 3D datasets. *J. Microsc.* **233**, 42–60.

Federici, F., Dupuy, L., Laplaze, L., Heisler, M. and Haseloff, J. (2012) Integrated genetic and computation methods for *in planta* cytometry. *Nat. Methods*, **9**, 483–485.

Fowlkes, C.C., Hendriks, C.L.L., Keränen, S.V. *et al.* (2008) A quantitative spatiotemporal atlas of gene expression in the *Drosophila* blastoderm. *Cell*, **133**, 364–374.

Friml, J., Benkov, E., Blilou, I. *et al.* (2002) AtPIN4 mediates sink-driven auxin gradients and root patterning in Arabidopsis. *Cell*, **108**, 661–673.

Fujie, M., Kuroiwa, H., Kawano, S. and Tsuneyoshi, K. (1993) Studies on the behavior of organelles and their nucleoids in the root apical meristem of *Arabidopsis thaliana* (L.) Col. *Planta*, **189**, 443–452.

Helariutta, Y., Fukaki, H., Wysocka-Diller, J., Nakajima, K., Jung, J., Sena, G. and Benfey, P.N. (2000) The *SHORT-ROOT* gene controls radial patterning of the Arabidopsis root through radial signaling. *Cell*, **101**, 555–567.

Lein, E.S., Hawrylycz, M.J., Ao, N. *et al.* (2007) Genome-wide atlas of gene expression in the adult mouse brain. *Nature*, **445**, 168–176.

Long, F., Peng, H., Liu, X., Kim, S.K. and Myers, E. (2009) A 3D digital atlas of *C. elegans* and its application to single-cell analyses. *Nat. Methods*, **6**, 667–672.

Lowe, D.G. (2004) Distinctive image features from scale-invariant keypoints. *Int. J. Comp. Vision*, **60**, 91–110.

Luengo Hendriks, C.L., Keränen, S.V., Fowlkes, C.C. *et al.* (2006) Three-dimensional morphology and gene expression in the *Drosophila* blastoderm at cellular resolution. I: data acquisition pipeline. *Genome Biol.* **7**, R123.

Malamy, J.E. and Benfey, P.N. (1997) Organization and cell differentiation in lateral roots of *Arabidopsis thaliana*. *Development*, **124**, 33–44.

Müller, A., Guan, C., Gälweiler, L., Tänzler, P., Huijser, P., Marchant, A., Parry, G., Bennett, M., Wisman, E. and Palme, K. (1998) *AtPIN2* defines a locus of *Arabidopsis* for root gravitropism control. *EMBO J.* **17**, 6903–6911.

Ottenschläger, I., Wolff, P., Wolverton, C., Bhalerao, R.P., Sandberg, G., Ishikawa, H., Evans, M. and Palme, K. (2003) Gravity-regulated differential auxin transport from columella to lateral root cap cells. *Proc. Natl Acad. Sci. USA*, **100**, 2987–2991.

Paponov, I.A., Teale, W.D., Trebar, M., Blilou, I. and Palme, K. (2005) The PIN auxin efflux facilitators: evolutionary and functional perspectives. *Trends Plant Sci.* **10**, 170–177.

Petrášek, J., Mravec, J., Bouchard, R., *et al.* (2006) PIN proteins perform a rate-limiting function in cellular auxin efflux. *Science*, **312**, 914–918.

Ronneberger, O., Liu, K., Rath, M. *et al.* (2012) ViBE–Z: a framework for 3D virtual colocalization analysis in zebrafish larval brains. *Nat. Methods*, **9**, 735–742.

Santuari, L., Scacchi, E., Rodriguez-Villalon, A., Salinas, P., Dohmann, E.M., Brunoud, G., Vernoux, T., Smith, R.S. and Hardtke, C.S. (2011) Positional information by differential endocytosis splits auxin response to drive Arabidopsis root meristem growth. *Curr. Biol.* **21**, 1918–1923.

Schmidt, T., Keuper, M., Pasternak, T., Palme, K. and Ronneberger, O. (2012) Modeling of sparsely sampled tubular surfaces using coupled curves. *Lect. Notes Comput. Sci.* **7476**, 83–92.

Schulz, J., Schmidt, T., Ronneberger, O., Burkhardt, H., Pasternak, T., Dovzhenko, A. and Palme, K. (2006) Fast scalar and vectorial grayscale based invariant features for 3D cell nuclei localization and classification. *Lect. Notes Comput. Sci.* **4174**, 182–191.

Sena, G., Frentz, Z., Birnbaum, K.D. and Leibler, S. (2011) Quantitation of cellular dynamics in growing Arabidopsis roots with light sheet microscopy. *PLoS ONE*, **6**, e21303.

Shaw, S.L. and Ehrhardt, D.W. (2013) Smaller, faster, brighter: advances in optical imaging of living plant cells. *Annu. Rev. Plant Biol.* **64**, 351–375.

Skibbe, H., Reisert, M., Schmidt, T., Brox, T., Ronneberger, O. and Burkhardt, H. (2012) Fast rotation invariant 3D feature computation utilizing efficient local neighborhood operators. *IEEE Trans. Pattern Anal. Mach. Intell.* **34**, 1563–1575.

Truernit, E., Bauby, H., Dubreucq, B., Grandjean, O., Runions, J., Barthélémy, J. and Palauqui, J.-C. (2008) High-resolution whole-mount imaging of three-dimensional tissue organization and gene expression enables the study of phloem development and structure in Arabidopsis. *Plant Cell*, **20**, 1494–1503.

Ubeda-Tomás, S., Federici, F., Casimiro, I., Beemster, G.T., Bhalerao, R., Swarup, R., Doerner, P., Haseloff, J. and Bennett, M.J. (2009) Gibberellin signaling in the endodermis controls arabidopsis root meristem size. *Curr. Biol.* **19**, 1194–1199.

Vapnik, V.N. (1998) *Statistical Learning Theory*. Oxford, UK: Wiley Interscience.

Wuyts, N., Palauqui, J.-J., Conejero, G., Verdeil, J.-L., Granier, C. and Massonnet, C. (2010) High-contrast three-dimensional imaging of the Arabidopsis leaf enables the analysis of cell dimensions in the epidermis and mesophyll. *Plant Methods*, **6**, 17.

© 2014 The Authors

1365313x, 2014, 5, Downloaded from https://onlinelibrary.wiley.com/doi/10.1111/tpj.12429 by Cochrane France, Wiley Online Library on [21/10/2026]. See the Terms and Conditions (https://onlinelibrary.wiley.com/terms-and-conditions) on Wiley Online Library for rules of use; OA articles are governed by the applicable Creative Commons License